

Spike Imaging Velocimetry: Dense Motion Estimation of Fluids Using Spike Streams

Yunzhong Zhang, Bo Xiong, You Zhou, Changqing Su,
Zhen Cheng, Zhaofei Yu, Xun Cao, Tiejun Huang

Abstract

Particle Image Velocimetry (PIV) is a widely adopted non-invasive imaging technique that tracks the motion of tracer particles across image sequences to capture the velocity distribution of fluid flows. It is commonly employed to analyze complex flow structures and validate numerical simulations. This study explores the untapped potential of spike cameras—ultra-high-speed, high-dynamic-range vision sensors—in high-speed fluid velocimetry. We propose a deep learning framework, Spike Imaging Velocimetry (SIV), tailored for high-resolution fluid motion estimation. To enhance the network’s performance, we design three novel modules specifically adapted to the characteristics of fluid dynamics and spike streams: the Detail-Preserving Hierarchical Transform (DPHT), the Graph Encoder (GE), and the Multi-scale Velocity Refinement (MSVR). Furthermore, we introduce a spike-based PIV dataset, Particle Scenes with Spike and Displacement (PSSD), comprising labeled samples from three representative scenarios in fluid dynamics. Our proposed method outperforms existing baselines on the PSSD dataset, demonstrating its effectiveness. The implementation details of our project, including code and configuration settings, are provided in the supplementary material.

Abstract

Particle Image Velocimetry (PIV) is a widely adopted non-invasive imaging technique that tracks the motion of tracer particles across image sequences to capture the velocity distribution of fluid flows. It is commonly employed to analyze complex flow structures and validate numerical simulations. This study explores the untapped potential of spike cameras—ultra-high-speed, high-dynamic-range vision sensors—in high-speed fluid velocimetry. We propose a deep learning framework, Spike Imaging Velocimetry (SIV), tailored for high-resolution fluid motion estimation. To enhance the network’s performance, we design three novel modules specifically adapted to the characteristics of fluid dynamics and spike streams: the Detail-Preserving Hierarchical Transform (DPHT), the Graph Encoder (GE), and the Multi-scale Velocity Refinement (MSVR). Furthermore, we introduce a spike-based PIV dataset, Particle Scenes with Spike and Displacement (PSSD), comprising labeled samples from three representative scenarios in fluid dynamics. Our proposed method outperforms existing baselines on the PSSD dataset, demonstrating its effectiveness. The implementation details

of our project, including code and configuration settings, are provided in the supplementary material.

Introduction

The need for accurate and non-invasive flow measurement methods has led to the widespread adoption of Particle Image Velocimetry (PIV), a powerful diagnostic tool in fluid dynamics research. This technique has been widely applied to critical topics such as studying the aerodynamic shapes of aircraft (Kompenhans et al. 2000), optimizing vehicle designs to reduce air resistance (Nakagawa et al. 2016), improving energy conversion efficiency in combustion processes (Chen, Li, and Zhu 2022), understanding the impact of blood flow dynamics on diseases (Raschi et al. 2012), and predicting the spread of water pollution (MoayeriKashani et al. 2016). In PIV experiments or simulations,

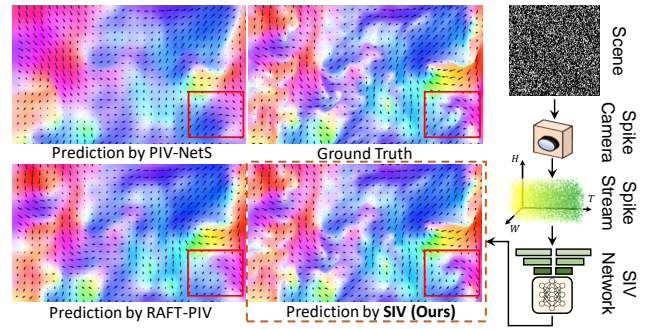


Figure 1: A schematic of fluid velocity field estimation based on spike cameras, and a comparison of the complex velocity field estimated using our proposed SIV network with PIV-NetS (Cai et al. 2019b) and RAFT-PIV (Lagemann et al. 2021).

tracer particles (e.g., silver-coated particles) are introduced into the fluid to scatter optical signals. By estimating their displacements, PIV can infer the velocities of the fluid in which they are suspended. The success of optical flow networks (Dosovitskiy et al. 2015; Sun et al. 2018; Teed and Deng 2020) has inspired the development of learning-based PIV algorithms (Cai et al. 2019b,a; Lagemann et al. 2021). Although optical flow networks generally exhibit good

generalization ability, the characteristics of fluid scenes cannot be ignored for further performance improvement. Turbulence is an irregular flow phenomenon occurring at high Reynolds numbers. When measuring the turbulent velocity field with PIV, this scenario is significantly different from macroscopic worlds, with the following key challenges:

- (1) The fluid often moves rapidly within the field of view.
- (2) The scene contains extensive empty regions without tracer particles, yet the network is required to estimate the full flow field.
- (3) Unlike solids, the fluid is highly sparse and unstructured overall, despite the presence of vortices of different scales (called quasi-order structures).

These challenges often coexist in turbulence. Challenge (1) places high demands on the experimental hardware, typically requiring ultra-high-speed cameras. Challenge (2) requires addressing potential resolution loss in the network carefully. Challenge (3) introduces problems to the extraction of context features. To address these challenges, we propose improvements in both hardware and algorithm aspects.

In terms of hardware, we explore the application of spike cameras (a type of neuromorphic camera) for PIV. We argue that using spike cameras in fluid measurement tasks offers several advantages:

High temporal resolution (HTR). Spike cameras can achieve ultra-high temporal resolution (20000Hz), reducing the interval Δt between the source and target time, and providing rich temporal information for accurate predictions. This enables spike cameras to handle Challenge (1) effectively;

High dynamic range (HDR). When particles accumulate in large numbers, local regions may become overly bright, exceeding the dynamic range of conventional cameras. Spike cameras asynchronously accumulate photons at each pixel, inherently possessing a much larger dynamic range. This makes them more advantageous in scenarios with uneven brightness (such as inappropriate lighting or particles moving toward concentrated regions);

Reduced experimental complexity. Spike cameras can continuously capture images at high frame rates with exceptionally low bandwidth and eliminate the need for synchronization controllers to modulate the camera and laser.

We propose a specialized network, **Spike Imaging Velocimetry (SIV)**, for estimating fluid velocity fields. To enhance network performance, we develop three novel modules tailored to the characteristics of fluid dynamics and spike cameras. These include the **Detail-Preserving Hierarchical Transform (DPHT)**, which enhances feature extraction from spike streams while mitigating downsampling artifacts; the **Graph Encoder (GE)**, which maps features into a graph structure for adaptive context aggregation; and the **Multi-scale Velocity Refinement (MSVR)**, which addresses over-smoothing in predicted flow fields.

We also introduce a new dataset, **Particle Scenes with Spike and Displacement (PSSD)**, designed for learning fluid motion from spike data. It covers three representative motion estimation scenarios: steady turbulence, high-speed

flow, and high dynamic range conditions.

Extensive experiments demonstrate the superiority of SIV over both image-based and spike-based baselines. SIV achieves state-of-the-art performance across all evaluation settings. The effectiveness of each proposed module is further validated through ablation studies.

The main contributions of this work are summarized as follows:

1. We explore a feasible solution for applying spike cameras to fluid velocity measurement, opening new directions for PIV.
2. We design a dedicated network, SIV, tailored to fluid dynamics and turbulent flow properties, and propose three novel modules: the DPHT, GE, and MSVR.
3. We propose a new dataset, PSSD, which captures continuous fluid motion across four flow types and three challenging experimental scenarios.
4. We conduct extensive quantitative experiments and qualitative visual comparisons, demonstrating that SIV achieves state-of-the-art performance across multiple benchmarks. We further perform ablation studies to systematically validate the effectiveness of each proposed module.

Related Work

Spike-based Optical Flow Estimation

The spike camera (Dong, Huang, and Tian 2021; Huang 2019) is a type of neuromorphic camera (NeurCam). Inspired by biological visual neural structures and mechanisms, NeurCams emulate the encoding principles of the primate retina. Spike cameras mimic the encoding principles of the central fovea in the retina, providing continuous visual information with ultra-high temporal resolutions, high dynamic range(HDR), and significantly reduced energy consumption and latency, making them well-suited for high-speed motion scenarios. Their pixels independently accumulate photons and emit a spike when the accumulated intensity exceeds a certain threshold. This process maps the incoming photon stream into the spike stream, which preserves spatiotemporal relationships and can be reconstructed into images. For a detailed explanation of the working mechanism, refer to (Dong, Huang, and Tian 2021). The application of spike cameras in optical flow estimation provides significant insights for this study. Although optical flow estimation is generally used to estimate the motion of macroscopic objects, its principles and objectives are aligned with those of PIV. The techniques employed in PIV for image registration and displacement estimation are essentially a variant of optical flow estimation. Spike-based optical flow estimation is still a relatively new field. (Hu et al. 2022) introduced a specialized neural network architecture for spike-based optical flow estimation. This structure can adaptively eliminate motion blur in spike streams based on prior motion information. A framework based on RAFT is proposed by (Zhao et al. 2022) to handle continuous spike streams. (Zhao et al. 2024) demonstrates that using a multi-layer hierarchical structure to characterize spike streams can effectively suppress the influence of randomness in spikes and enhance the feature extraction capability of the network.

(Chen, Yu, and Huang 2023) proposed a self-supervised approach to learn optical flow from spike cameras, which is then extended by (Xia et al. 2024).

Image-based PIV Algorithms

Many traditional image-based PIV algorithms (Lourenco and Krothapalli 1995; Nobach and Honkanen 2005) usually involve applying a fast Fourier transform (FFT) between two subregions of image pairs, known as interrogation windows. Displacement is then determined by finding the maximum correlation between the two interrogation windows, which is similar to the correlation method in optical flow estimation to some extent. However, traditional methods depend on finely tuned parameters and complex optimization techniques. With advancements in optical flow networks, various architectures (Dosovitskiy et al. 2015; Sun et al. 2018; Teed and Deng 2020) have been developed to predict dense velocity fields of macroscopic objects with high accuracy. Early PIV networks like PIV-DCNN (Lee, Yang, and Yin 2017) laid the groundwork for these developments. PIV-NetS (Cai et al. 2019b) is capable of generating full-resolution displacement outputs. (Cai et al. 2019a) adapt LiteFlowNet (Hui, Tang, and Loy 2018) to PIV. RAFT-PIV (Lagemann et al. 2021), derived from RAFT (Teed and Deng 2020), has shown exceptional performance on multiple datasets. (Yu et al. 2021) removes the computationally inefficient components of RAFT, such as the context encoder, to improve inference speed. Additionally, unsupervised learning frameworks for PIV (Zhang and Piggott 2020; Zhang et al. 2023a) have been introduced, reducing reliance on the extremely difficult-to-obtain ground-truth displacements. Other recent PIV networks include LIMA (Manickathan, Mucignat, and Lunati 2023), CC-FCN (Gao et al. 2021), En-FlowNetC (Ji, An, and Hui 2024), ARAFT-FlowNet (Han and Wang 2023), OFVNetS (Ji, Hui, and An 2024), and PIV-PWCNet (Zhang et al. 2023b). However, the performance gains of most PIV networks are largely attributed to advances in optical flow estimation architectures, rather than targeted enhancements tailored to the specific characteristics of fluid dynamics, and most implementations remain unavailable as open-source.

Event-based PIV Algorithms

The event camera (Lichtsteiner, Posch, and Delbruck 2008; Moeys et al. 2017; Posch, Matolin, and Wohlgenannt 2010; Huang, Guo, and Chen 2017) is another type of NeurCam, which is inspired by the peripheral retina (Rebecq et al. 2019). Unlike spike cameras, event cameras independently monitor the change in light intensity (increase or decrease) at each pixel and generate signals based on the local pixel information of dynamic changes. When the brightness change of a pixel exceeds a preset threshold, the camera records this change event (brightness increase as a positive event, brightness decrease as a negative event) and outputs its timestamp, position, and change value as data. However, due to the lack of absolute intensity values, event cameras struggle to reconstruct complete images, particularly in static regions and with fine textures. The application of event cameras to PIV has already been explored by (Willert and Klinner 2022) and

(Willert 2023). Similar to the spike camera, the event camera offers higher temporal resolution, high dynamic range, low latency, and reduced experimental complexity.

Preliminary

The Working Principle of the Spike Camera

Each photosensitive element in a spike camera generates spike streams sequentially over time. A "1" in the stream indicates that a spike has occurred (i.e., the threshold has been reached), while a "0" indicates an ongoing accumulation state. The Integral-and-Fire (IF) mechanism of spike cameras can be mathematically represented as follows:

$$A(\mathbf{x}, t) = \int_0^t \alpha \cdot I(\mathbf{x}, \tau) \bmod \theta, \quad (1)$$

Where $A(\mathbf{x}, t)$ represents the voltage of the accumulator at pixel $\mathbf{x} = (x, y)$ at time τ , and θ is the threshold of the comparator. The spike camera's output is a spatiotemporal binary stream S of size $H \times W \times N$, where H and W are the height and width of the sensor, respectively, and N represents the temporal dimension. Compared to traditional cameras, spike cameras preserve richer visual information regarding both temporal resolution and brightness representation.

Data Generation

Our proposed dataset, Particle Scenes with Spike and Displacement (PSSD), includes three sub-datasets: Steady Turbulence (Problem 1), High-speed Flow (Problem 2), and HDR Scenes (Problem 3). Each sub-dataset comprises 10,000 sample sequences of spike streams and the corresponding ground-truth turbulent velocity fields when $\Delta t = 21$ (approximately 1.05 ms) and $\Delta t = 11$ (approximately 0.55 ms). Additionally, we provide corresponding pairs of images for comparative analysis for image-based methods. We use the reference flow field to simulate the motion of the scene and construct a virtual spike camera to trigger the spike stream. The reference flow field data are taken from the high-precision numerical simulation database used for turbulence research, Johns Hopkins Turbulence Database (JHTDB) (Li et al. 2008). JHTDB employs Direct Numerical Simulation (DNS) to simulate turbulent flow fields. DNS directly solves the Navier-Stokes equations without any model assumptions or simplifications, enabling precise capture of all scales in turbulent flow. This method resolves the fluid motion in both space and time with high-resolution grids, accurately capturing the complex and multi-scale nature of turbulence. Additional details about the dataset can be found in our supplementary materials.

Approaches

Overall Architecture

Problem definition. Let $\mathbf{S} \in \mathbb{B}^{H \times W \times T}$ represent the spike stream recorded by the spike camera. \mathbb{B} is the binary domain. We aim to estimate the displacement \mathbf{D} of particles in the fluid between time moments t and $t + \Delta t$. At the pixel level,

for any given pixel $\mathbf{p} = (x, y)$ at t , we need to find a unique correspondence formulated by:

$$\mathcal{I}(\mathbf{p}, t) \leftarrow \mathcal{I}(\mathbf{p}, t + \Delta t). \quad (2)$$

Here, \mathcal{I} is the mapping of the spike stream \mathbf{S} in the high-dimensional feature space, representing the scene information.

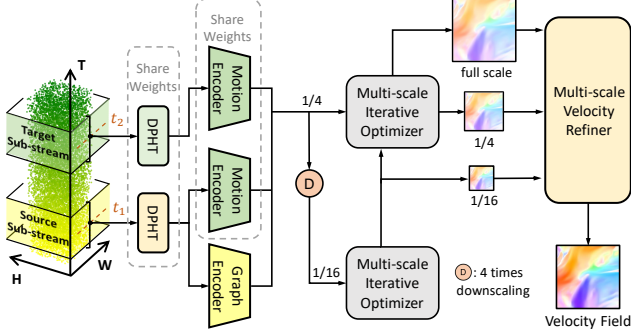


Figure 2: Spike Imaging Velocimetry (SIV) network.

Detail-Preserving Hierarchical Transform

In order to avoid the loss of particle signal information during feature extraction, we propose a multi-scale pyramidal architecture, named Detail-Preserving Hierarchical Transform (DPHT), which incorporates a 3D Detail-Preserving Downsampling module (as shown in Figure 3(a)).

3D Detail-Preserving downsampling. As shown in Figure 3(a), suppose the input of level l is a feature vector $\mathbf{x}^{(l)}$, and the processing of $\mathbf{x}^{(l)}$ at this level is as follows:

$$\mathbf{x}_{\text{out}}^{(l)} = \mathcal{D}^{(l)}(\mathbf{x}^{(l)}) = \mathcal{F}_{2C}(\mathcal{F}_{3C}(\mathbf{x}^{(l)}) + \mathcal{F}_{3MP}(\mathbf{x}^{(l)})), \quad (3)$$

Here, \mathcal{F}_{3C} represents a $5 \times 3 \times 3$ 3D convolution, \mathcal{F}_{3MP} is a combination of a 3D max pooling operation and a $5 \times 1 \times 1$ 3D convolution, and \mathcal{F}_{2C} refers to a sequential stack of 2D convolutions. The output of the previous level serves as the input to the next level, i.e., $\mathbf{x}^{(l+1)} = \mathbf{x}_{\text{out}}^{(l)} = \mathcal{D}^{(l)}(\mathbf{x}^{(l)})$.

Global temporal aggregation. In this step, the output feature vectors from each level are further refined by several convolutions (for detailed information, refer to the supplementary materials), and then concatenated together to form the final representation of the DPHT:

$$\mathbf{R} = \mathcal{A}_m[\text{Concat}(\mathbf{x}_{\text{out}}^{(l=1)}, \mathbf{x}_{\text{out}}^{(l=2)}, \mathbf{x}_{\text{out}}^{(l=3)})], \quad (4)$$

\mathcal{A}_m denotes convolution. After processing with DPHT, the signals of the source and target sub-streams are denoted as \mathbf{R}_s and \mathbf{R}_t , respectively.

Graph Encoder

When the Reynolds number is high, fluid flow becomes turbulent. As energy cascades and dissipates, large vortices become unstable and gradually break into smaller ones until they vanish. This indicates that fluid motion is not purely chaotic, but rather exhibits an underlying topological structure. To capture the contextual information of the fluid,

we propose a Graph Encoder (GE). It is a feature extraction network based on Graph Neural Networks (GNNs) and Convolutional Neural Networks (CNNs). By representing features as graph nodes and constructing a dynamic adjacency matrix, GE flexibly aggregates and updates information from neighboring nodes, enabling a larger receptive field than conventional CNNs. Graph Attention Networks (GATs) (Veličković et al. 2017), leveraging attention mechanisms, learn the relative contribution of each neighbor to a node’s new representation, thereby mitigating interference from particle-sparse regions. The serial combination of GNN and CNN enables adaptive global perception and local refinement, effectively capturing fluid-specific contextual features.

Graph projection. The first step is to map \mathbf{R}_s extracted from DPHT from the general coordinate space to the node space, i.e., $\mathbf{V}_c = \mathcal{P}_{R \rightarrow V}(\mathbf{R}_s)$. The mapped context node representations, denoted as $\mathbf{V}_c = \{v_c^1, \dots, v_c^n\} \in \mathbb{R}^{C \times K}$, contain appearance features related to the shape and regional information of the scene. C indicates channel number and K is a hyper-parameter representing the number of nodes. In this paper, we set $K = 128$. $\mathcal{P}_{R \rightarrow V}(\cdot)$ is a linear combination of feature vectors within the grid space, formulated by,

$$v_{c,i} = \mathcal{N}\left(\sum_{\forall j} z_{ij} \cdot \mathbf{R}_{s,j}\right). \quad (5)$$

Here, $\mathcal{N}(\cdot)$ is the L_2 -normalization function applied to the channel dimension of each node vector, and z_{ij} denotes the projection weights computed by a CNN, i.e., $z = \mathcal{F}_{R \rightarrow V}(\mathbf{R}_s) \in \mathbb{R}^{(H \times W) \times K}$.

Graph convolution layer. After obtaining the nodes \mathbf{v}_c in the graph space, the dynamic adjacency matrix $\tilde{\mathbf{A}} = \mathbf{V}_c^T \mathbf{V}_c$ can be derived by calculating the similarity between all node vectors. The detailed definition of GAT can be found in the supplementary material. Here, we implicitly denote the operations of the two GAT modules as \mathcal{G}_1 and \mathcal{G}_2 . The updated node features are given by

$$\mathbf{V}_c^{\text{out}} = \mathcal{G}_2[\mathcal{G}_1(\mathbf{V}_c, \tilde{\mathbf{A}}) + \mathbf{V}_c, \tilde{\mathbf{A}}] + \mathcal{G}_1(\mathbf{V}_c, \tilde{\mathbf{A}}) + \mathbf{V}_c, \quad (6)$$

Graph re-projection. Our graph re-projection operation $\mathcal{P}_{V \rightarrow R}(\cdot)$ takes the transformed vertex features $\mathbf{V}_c^{\text{out}}$ and the projection weight matrix $\mathbf{Z} = [z_{ij}]$ as inputs, generating a 2D feature map $\tilde{\mathbf{R}}_c$. Since inverting the projection weight matrix is not feasible, we follow the approach in (Li and Gupta 2018; Luo et al. 2022) and compute the enhanced grid context features $\tilde{\mathbf{R}}_c$ by re-weighting the vertex features $\mathbf{V}_c^{\text{out}}$. This is given by,

$$\tilde{\mathbf{R}}_c = \mathcal{P}_{V \rightarrow R}(\mathbf{V}_c^{\text{out}}, \mathbf{Z}) = \mathbf{Z} \mathbf{V}_c^{\text{out}T}. \quad (7)$$

Thus, $\mathcal{P}_{V \rightarrow R}$ linearly interpolates 2D pixel features based on the node assignments of the 2D grid features, without additional parameters. Note that even if two pixels are assigned to the same node, they will have different features after re-projection. Therefore, the GCU may preserve the spatial details of the signal. Finally, these projection results can be integrated into a residual extractor network \mathcal{R} for local refinement. Final context feature \mathbf{F}_c given by,

$$\mathbf{F}_c = \mathcal{R}(\mathbf{R}_s + \alpha \tilde{\mathbf{R}}_c), \quad (8)$$

Experimental Results

In this section, we evaluate our method on the PSSD dataset and compare its performance with other traditional and learning-based methods. Additionally, we conduct a series of ablation experiments to assess the effectiveness of the proposed modules.

Experimental Details

SIV is implemented using the PyTorch framework on a single NVIDIA RTX 2080 Ti GPU. We employ the Adam optimizer with a warm-up strategy during training. For each sub-dataset, we train the model for 100 epochs with an initial learning rate of 10^{-4} , applying an 85% decay every 10 epochs. The number of iterative refinements of GRUs is set to 12. The batch size is set to 4.

Following (Cai et al. 2019b) and (Lagemann et al. 2021), we use endpoint error (EPE) as the primary evaluation metric for comparing different algorithms. Additionally, we incorporate another widely used PIV metric, Root Mean Squared Error (RMSE), in our extensive experiments, as detailed in the supplementary material.

Comparative Experiments

We compare our method against several open-source baselines, including a classical PIV algorithm (Cai et al. 2018), PIV networks (PIV-NetS (Cai et al. 2019b), RAFT-PIV (Lagemann et al. 2021)), spike-adapted general optical flow networks (e.g., Flowformer with spike input (Huang et al. 2022)), and spike-based optical flow networks (SCFlow (Hu et al. 2022), HiST-SFlow (Zhao et al. 2024)).

As shown in Table 1, 2, and 3, $\Delta t = 21$ and $\Delta t = 11$ represent the number of timestamps for the central temporal intervals between two spike streams used for velocity field prediction, respectively. For detailed descriptions, please refer to the supplementary material. Our proposed SIV method achieves the lowest average End-Point Error (EPE) across all evaluated sub-datasets. Compared to baseline approaches, SIV demonstrates superior prediction accuracy in both low-velocity (Problem 1) and high-velocity (Problem 2) optical flow scenarios. Furthermore, in high dynamic range conditions (Problem 3), SIV effectively exploits the inherent advantages of spike-based input modalities to address the fundamental limitations of conventional frame-based imaging systems.

Figure 5 presents the visualized predictions of all methods across three datasets. The top row shows the velocity fields visualized using the standard optical flow color coding (Baker et al. 2011). The bottom row shows the endpoint error (EPE) maps between the predicted and ground-truth flow. Shear layers are often a primary source of turbulence generation and development. SIV achieves the lowest prediction error in both shear layers and small-scale vortices, while avoiding noticeable blurring, distortion, or discontinuities.

Ablation Study

Ablation of modules. We conduct a series of ablation experiments to evaluate the contribution of each component to

overall performance, as detailed in Table 4. All the values are the arithmetic mean of the scenes. The best results are marked in bold. These results underscore the effectiveness of the DPHT, GE, MSVR and L_{grad} . In Table 4, the comparison between experiments (A) and (B) demonstrates the effectiveness of DPHT. Both the comparison between (B) and (C) and that between (D) and (E) demonstrate the effectiveness of the Graph Encoder (GE). Both the comparison between (B) and (D) and that between (C) and (E) highlight the contribution of MSVR.

Ablation of β . Table 5 summarizes the ablation study on the weighting coefficient β of the proposed loss function. The results indicate that setting $\beta = 0.3$ yields the best performance for the current model and dataset. Additional ablation studies are provided in the supplementary material.

Conclusion

We explore a novel approach to fluid motion estimation using spike cameras and propose a specialized network architecture, termed Spike Imaging Velocimetry (SIV), designed to solve PIV tasks while adapting to the scenario-specific characteristics of fluid scenes. We propose a Detail-Preserving Hierarchical Transform module to preserve particle signal information during the pre-processing of spike streams. We design a Graph Encoder to extract contextual features from highly unstructured and turbulent flow fields. We develop a Multi-scale Velocity Refinement module to refine the velocity field. We also introduce a challenging and realistic PIV dataset, named Particle Scenes with Spike and Displacement (PSSD). Experimental results demonstrate that our method achieves state-of-the-art performance on the PSSD dataset and accurately estimates velocities in small-scale yet critical flow structures such as shear layers and vortices. In summary, this study demonstrates the potential of spike cameras in fluid velocity measurement and offers new perspectives and directions for PIV network design.

References

- Baker, S.; Scharstein, D.; Lewis, J. P.; Roth, S.; Black, M. J.; and Szeliski, R. 2011. A database and evaluation methodology for optical flow. *International journal of computer vision*, 92: 1–31.
- Cai, S.; Liang, J.; Gao, Q.; Xu, C.; and Wei, R. 2019a. Particle image velocimetry based on a deep learning motion estimator. *IEEE Transactions on Instrumentation and Measurement*, 69(6): 3538–3554.
- Cai, S.; Mémin, E.; Dérian, P.; and Xu, C. 2018. Motion estimation under location uncertainty for turbulent fluid flows. *Experiments in Fluids*, 59(1): 8.
- Cai, S.; Zhou, S.; Xu, C.; and Gao, Q. 2019b. Dense motion estimation of particle images via a convolutional neural network. *Experiments in Fluids*, 60: 1–16.
- Chen, B.; Li, X.; and Zhu, Z. 2022. Investigations of energy distribution and loss characterization in a centrifugal impeller through PIV experiment. *Ocean Engineering*, 247: 110773.

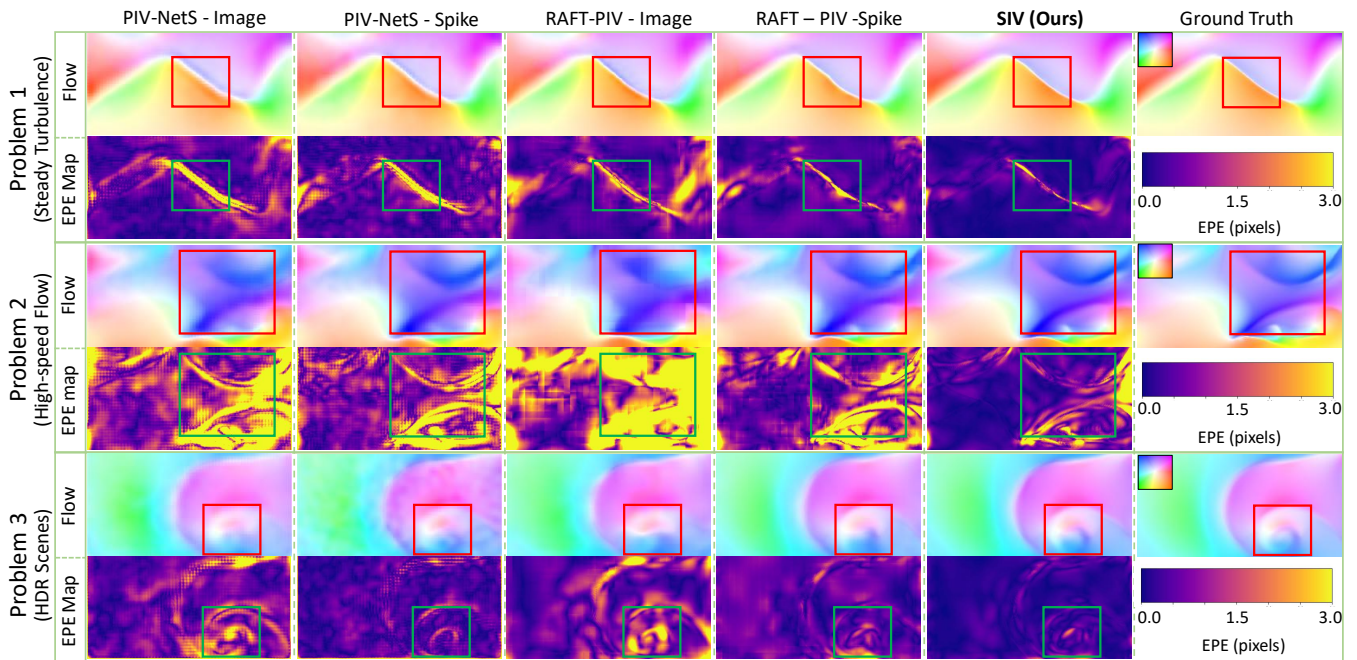


Figure 5: Visualization examples of different algorithms in Steady Turbulence (Problem 1), High-speed Flow (Problem 2), and HDR Scenes (Problem 3) are shown. For each problem, the red box in the top optical flow map and the green box in the bottom EPE error map indicate the same region of the flow field.

| Methods | Channel | | Isotropic | | Mhd | | Mixing | | Average | |
|-------------------|---------------|---------------|---------------|---------------|---------------|---------------|---------------|---------------|---------------|---------------|
| | $\Delta t=21$ | $\Delta t=11$ |
| coarse-to-fine HS | 6.790 | 0.509 | 7.415 | 1.998 | 7.683 | 2.558 | 9.388 | 1.954 | 7.819 | 1.755 |
| RAFT-PIV-Image | 0.377 | 0.215 | 2.181 | 1.252 | 1.336 | 0.842 | 1.875 | 1.064 | 1.442 | 0.843 |
| RAFT-PIV-Spike | 0.347 | 0.208 | 1.223 | 0.755 | 0.857 | 0.557 | 0.958 | 0.581 | 0.846 | 0.525 |
| PIV-NetS-Image | 0.545 | 0.301 | 2.560 | 1.497 | 1.574 | 0.985 | 2.247 | 1.320 | 1.731 | 1.026 |
| PIV-NetS-Spike | 0.553 | 0.289 | 1.507 | 0.874 | 1.252 | 0.734 | 1.382 | 0.782 | 1.173 | 0.670 |
| SCFlow | 0.354 | 0.222 | 2.232 | 1.305 | 1.374 | 0.901 | 2.132 | 1.169 | 1.522 | 0.899 |
| HiST-SFlow | 0.369 | 0.224 | 1.271 | 0.796 | 0.964 | 0.611 | 1.029 | 0.637 | 0.908 | 0.567 |
| Flowformer-Spike | 0.286 | 0.147 | 1.069 | 0.642 | 0.727 | 0.437 | 0.806 | 0.472 | 0.722 | 0.425 |
| SIV (ours) | 0.239 | 0.159 | 0.896 | 0.587 | 0.613 | 0.422 | 0.680 | 0.441 | 0.607 | 0.402 |

Table 1: EPE (\downarrow) results on PSSD dataset (Problem 1). The best results are marked in bold.

Chen, S.; Yu, Z.; and Huang, T. 2023. Self-supervised joint dynamic scene reconstruction and optical flow estimation for spiking camera. In *Proceedings of the AAAI Conference on Artificial Intelligence*, volume 37, 350–358.

Dong, S.; Huang, T.; and Tian, Y. 2021. Spike camera and its coding methods. *arXiv preprint arXiv:2104.04669*.

Dosovitskiy, A.; Fischer, P.; Ilg, E.; Hausser, P.; Hazirbas, C.; Golkov, V.; Van Der Smagt, P.; Cremers, D.; and Brox, T. 2015. FlowNet: Learning optical flow with convolutional networks. In *Proceedings of the IEEE international conference on computer vision*, 2758–2766.

Gao, Q.; Lin, H.; Tu, H.; Zhu, H.; Wei, R.; Zhang, G.; and Shao, X. 2021. A robust single-pixel particle image velocimetry based on fully convolutional networks with cross-correlation embedded. *Physics of Fluids*, 33(12).

Han, Y.; and Wang, Q. 2023. An attention-mechanism in-

corporated deep recurrent optical flow network for particle image velocimetry. *Physics of Fluids*, 35(7).

Hu, L.; Zhao, R.; Ding, Z.; Ma, L.; Shi, B.; Xiong, R.; and Huang, T. 2022. Optical flow estimation for spiking camera. In *Proceedings of the IEEE/CVF Conference on Computer Vision and Pattern Recognition*, 17844–17853.

Huang, J.; Guo, M.; and Chen, S. 2017. A dynamic vision sensor with direct logarithmic output and full-frame picture-on-demand. In *2017 IEEE International Symposium on Circuits and Systems (ISCAS)*, 1–4. IEEE.

Huang, T. 2019. Method and device for encoding space-time signals. US Patent 10,523,972.

Huang, Z.; Shi, X.; Zhang, C.; Wang, Q.; Cheung, K. C.; Qin, H.; Dai, J.; and Li, H. 2022. Flowformer: A transformer architecture for optical flow. In *European conference on computer vision*, 668–685. Springer.

Hui, T.-W.; Tang, X.; and Loy, C. C. 2018. LiteflowNet:

| Methods | Channel | | Isotropic | | Mhd | | Mixing | | Average | |
|-------------------|---------------|---------------|---------------|---------------|---------------|---------------|---------------|---------------|---------------|---------------|
| | $\Delta t=21$ | $\Delta t=11$ |
| coarse-to-fine HS | 20.691 | 8.244 | 17.164 | 8.051 | 17.469 | 8.170 | 17.131 | 7.936 | 18.114 | 8.100 |
| RAFT-PIV-Image | 0.665 | 0.368 | 4.730 | 2.635 | 2.320 | 1.366 | 4.305 | 2.368 | 3.005 | 1.684 |
| RAFT-PIV-Spike | 0.688 | 0.412 | 2.410 | 1.483 | 1.468 | 0.959 | 2.071 | 1.241 | 1.659 | 1.024 |
| PIV-NetS-Image | 1.163 | 0.683 | 4.866 | 2.830 | 2.673 | 1.643 | 4.347 | 2.500 | 3.262 | 1.914 |
| PIV-NetS-Spike | 0.887 | 0.540 | 3.172 | 1.818 | 2.392 | 1.410 | 3.067 | 1.744 | 2.379 | 1.378 |
| SCFlow | 0.694 | 0.403 | 4.689 | 2.613 | 2.387 | 1.391 | 4.326 | 2.380 | 3.024 | 1.696 |
| HiST-SFlow | 0.556 | 0.364 | 2.212 | 1.365 | 1.404 | 0.998 | 1.911 | 1.179 | 1.521 | 0.976 |
| Flowformer-Spike | 0.533 | 0.284 | 1.975 | 1.179 | 1.214 | 0.748 | 1.668 | 0.972 | 1.348 | 0.796 |
| SIV (ours) | 0.370 | 0.254 | 1.687 | 1.080 | 1.071 | 0.722 | 1.449 | 0.912 | 1.144 | 0.742 |

Table 2: EPE (\downarrow) results on PSSD dataset (Problem 2). The best results are marked in bold.

| Methods | Channel | | Isotropic | | Mhd | | Mixing | | Average | |
|-------------------|---------------|---------------|---------------|---------------|---------------|---------------|---------------|---------------|---------------|---------------|
| | $\Delta t=21$ | $\Delta t=11$ |
| coarse-to-fine HS | 7.908 | 1.044 | 7.924 | 2.706 | 8.345 | 3.130 | 7.854 | 2.716 | 8.008 | 2.399 |
| RAFT-PIV-Image | 0.447 | 0.244 | 2.694 | 1.495 | 1.447 | 0.888 | 2.311 | 1.271 | 1.725 | 0.974 |
| RAFT-PIV-Spike | 0.320 | 0.200 | 1.203 | 0.740 | 0.798 | 0.530 | 0.946 | 0.576 | 0.817 | 0.512 |
| PIV-NetS-Image | 0.667 | 0.343 | 2.786 | 1.602 | 1.641 | 0.956 | 2.393 | 1.378 | 1.872 | 1.070 |
| PIV-NetS-Spike | 0.476 | 0.247 | 1.420 | 0.856 | 1.157 | 0.716 | 1.342 | 0.774 | 1.099 | 0.648 |
| SCFlow | 0.462 | 0.269 | 1.850 | 0.837 | 1.300 | 0.774 | 1.972 | 0.769 | 1.396 | 0.662 |
| HiST-SFlow | 0.329 | 0.180 | 1.179 | 0.640 | 0.832 | 0.452 | 0.960 | 0.476 | 0.825 | 0.437 |
| Flowformer-Spike | 0.269 | 0.145 | 1.052 | 0.620 | 0.716 | 0.429 | 0.813 | 0.481 | 0.713 | 0.419 |
| SIV (ours) | 0.234 | 0.155 | 0.880 | 0.573 | 0.598 | 0.404 | 0.677 | 0.438 | 0.598 | 0.392 |

Table 3: EPE (\downarrow) results on PSSD dataset (Problem 3). The best results are marked in bold.

| # | Settings | | | Problem 1 | Problem 2 | Problem 3 |
|-----|----------|----|------|---------------|---------------|---------------|
| | DPHT | GE | MSVR | $\Delta t=21$ | $\Delta t=21$ | $\Delta t=21$ |
| (A) | × | × | × | 0.805 | 1.450 | 0.776 |
| (B) | ✓ | × | × | 0.701 | 1.299 | 0.659 |
| (C) | ✓ | ✓ | × | 0.625 | 1.167 | 0.616 |
| (D) | ✓ | × | ✓ | 0.644 | 1.268 | 0.635 |
| (E) | ✓ | ✓ | ✓ | 0.607 | 1.144 | 0.598 |

Table 4: Ablation study of proposed modules, showing results for EPE (\downarrow). ✓ indicates module presence, × indicates absence. Setting (G) is our final model.

| # | β | Problem 1 | Problem 2 | Problem 3 |
|-----|---------|--------------|--------------|--------------|
| (A) | 0.0 | 0.620 | 1.169 | 0.615 |
| (B) | 0.1 | 0.617 | 1.163 | 0.605 |
| (C) | 0.2 | 0.615 | 1.157 | 0.603 |
| (D) | 0.3 | 0.607 | 1.144 | 0.598 |
| (E) | 0.4 | 0.613 | 1.146 | 0.610 |
| (F) | 0.5 | 0.619 | 1.141 | 0.617 |

Table 5: Ablation study of β , showing results for EPE (\downarrow).

A lightweight convolutional neural network for optical flow estimation. In *Proceedings of the IEEE conference on computer vision and pattern recognition*, 8981–8989.

Ji, K.; An, Q.; and Hui, X. 2024. Cross-correlation-based convolutional neural network with velocity regularization for high-resolution velocimetry of particle images. *Physics of Fluids*, 36(7).

Ji, K.; Hui, X.; and An, Q. 2024. Effects of velocity regular-

ization on neural network performance in processing particle images. *Physics of Fluids*, 36(10).

Kompenhans, J.; Raffel, M.; Dieterle, L.; Dewhurst, T.; Vollmers, H.; Ehrenfried, K.; Willert, C.; Pengel, K.; Kähler, C.; Schröder, A.; et al. 2000. Particle image velocimetry in aerodynamics: Technology and applications in wind tunnels. *Journal of Visualization*, 2(3-4): 229–244.

Lagemann, C.; Lagemann, K.; Mukherjee, S.; and Schröder, W. 2021. Deep recurrent optical flow learning for particle image velocimetry data. *Nature Machine Intelligence*, 3(7): 641–651.

Lee, Y.; Yang, H.; and Yin, Z. 2017. PIV-DCNN: cascaded deep convolutional neural networks for particle image velocimetry. *Experiments in Fluids*, 58: 1–10.

Li, Y.; and Gupta, A. 2018. Beyond grids: Learning graph representations for visual recognition. *Advances in neural information processing systems*, 31.

Li, Y.; Perlman, E.; Wan, M.; Yang, Y.; Meneveau, C.; Burns, R.; Chen, S.; Szalay, A.; and Eyink, G. 2008. A public turbulence database cluster and applications to study Lagrangian evolution of velocity increments in turbulence. *Journal of Turbulence*, 9(N31).

Lichtsteiner, P.; Posch, C.; and Delbruck, T. 2008. A 128×128 120 dB 15 μ s Latency Asynchronous Temporal Contrast Vision Sensor. *IEEE Journal of Solid-State Circuits*, 43(2): 566–576.

Lourenco, L.; and Krothapalli, A. 1995. On the accuracy of velocity and vorticity measurements with PIV. *Experiments in fluids*, 18(6): 421–428.

Luo, A.; Yang, F.; Luo, K.; Li, X.; Fan, H.; and Liu, S. 2022. Learning optical flow with adaptive graph reasoning. In *Pro-*

- ceedings of the AAAI conference on artificial intelligence, volume 36, 1890–1898.
- Manickathan, L.; Mucignat, C.; and Lunati, I. 2023. A lightweight neural network designed for fluid velocimetry. *Experiments in Fluids*, 64(10): 161.
- MoayeriKashani, M.; Lai, S.; Ibrahim, S.; Sulaiman, N.; and Teo, F. 2016. Tracking the hydrodynamic behavior of fine sediment using particle image velocimetry. *Environmental Earth Sciences*, 75: 1–13.
- Moeys, D. P.; Corradi, F.; Li, C.; Bamford, S. A.; Longinotti, L.; Voigt, F. F.; Berry, S.; Taverni, G.; Helmchen, F.; and Delbruck, T. 2017. A sensitive dynamic and active pixel vision sensor for color or neural imaging applications. *IEEE transactions on biomedical circuits and systems*, 12(1): 123–136.
- Nakagawa, M.; Kallweit, S.; Michaux, F.; and Hojo, T. 2016. Typical velocity fields and vortical structures around a formula one car, based on experimental investigations using particle image velocimetry. *SAE International Journal of Passenger Cars-Mechanical Systems*, 9(2016-01-1611): 754–771.
- Nobach, H.; and Honkanen, M. 2005. Two-dimensional Gaussian regression for sub-pixel displacement estimation in particle image velocimetry or particle position estimation in particle tracking velocimetry. *Experiments in fluids*, 38: 511–515.
- Posch, C.; Matolin, D.; and Wohlgenannt, R. 2010. A QVGA 143 dB dynamic range frame-free PWM image sensor with lossless pixel-level video compression and time-domain CDS. *IEEE Journal of Solid-State Circuits*, 46(1): 259–275.
- Raschi, M.; Mut, F.; Byrne, G.; Putman, C. M.; Tateshima, S.; Viñuela, F.; Tanoue, T.; Tanishita, K.; and Cebal, J. R. 2012. CFD and PIV analysis of hemodynamics in a growing intracranial aneurysm. *International journal for numerical methods in biomedical engineering*, 28(2): 214–228.
- Rebecq, H.; Ranftl, R.; Koltun, V.; and Scaramuzza, D. 2019. High speed and high dynamic range video with an event camera. *IEEE transactions on pattern analysis and machine intelligence*, 43(6): 1964–1980.
- Sun, D.; Yang, X.; Liu, M.-Y.; and Kautz, J. 2018. Pwcnnet: Cnns for optical flow using pyramid, warping, and cost volume. In *Proceedings of the IEEE conference on computer vision and pattern recognition*, 8934–8943.
- Teed, Z.; and Deng, J. 2020. Raft: Recurrent all-pairs field transforms for optical flow. In *Computer Vision—ECCV 2020: 16th European Conference, Glasgow, UK, August 23–28, 2020, Proceedings, Part II 16*, 402–419. Springer.
- Veličković, P.; Cucurull, G.; Casanova, A.; Romero, A.; Lio, P.; and Bengio, Y. 2017. Graph attention networks. *arXiv preprint arXiv:1710.10903*.
- Willert, C. E. 2023. Event-based imaging velocimetry using pulsed illumination. *Experiments in Fluids*, 64(5): 98.
- Willert, C. E.; and Klinner, J. 2022. Event-based imaging velocimetry: an assessment of event-based cameras for the measurement of fluid flows. *Experiments in Fluids*, 63(6): 101.
- Xia, L.; Ding, Z.; Zhao, R.; Zhang, J.; Ma, L.; Yu, Z.; Huang, T.; and Xiong, R. 2024. Unsupervised optical flow estimation with dynamic timing representation for spike camera. *Advances in Neural Information Processing Systems*, 36.
- Yu, C.; Bi, X.; Fan, Y.; Han, Y.; and Kuai, Y. 2021. Light-PIVNet: An effective convolutional neural network for particle image velocimetry. *IEEE Transactions on Instrumentation and Measurement*, 70: 1–15.
- Zhang, M.; and Piggott, M. D. 2020. Unsupervised learning of particle image velocimetry. In *High Performance Computing: ISC High Performance 2020 International Workshops, Frankfurt, Germany, June 21–25, 2020, Revised Selected Papers 35*, 102–115. Springer.
- Zhang, W.; Dong, X.; Sun, Z.; and Xu, S. 2023a. An unsupervised deep learning model for dense velocity field reconstruction in particle image velocimetry (PIV) measurements. *Physics of Fluids*, 35(7).
- Zhang, W.; Nie, X.; Dong, X.; and Sun, Z. 2023b. Pyramidal deep-learning network for dense velocity field reconstruction in particle image velocimetry. *Experiments in Fluids*, 64(1): 12.
- Zhao, R.; Xiong, R.; Zhang, J.; Zhang, X.; Yu, Z.; and Huang, T. 2024. Optical Flow for Spike Camera with Hierarchical Spatial-Temporal Spike Fusion. In *Proceedings of the AAAI Conference on Artificial Intelligence*, 7496–7504.
- Zhao, R.; Xiong, R.; Zhao, J.; Yu, Z.; Fan, X.; and Huang, T. 2022. Learning optical flow from continuous spike streams. *Advances in Neural Information Processing Systems*, 35: 7905–7920.
- Zheng, Z.; Nie, N.; Ling, Z.; Xiong, P.; Liu, J.; Wang, H.; and Li, J. 2022. Dip: Deep inverse patchmatch for high-resolution optical flow. In *Proceedings of the IEEE/CVF Conference on Computer Vision and Pattern Recognition*, 8925–8934.